

A Laboratory Model of Exchange and Mixing between Western Boundary Layers and Subbasin Recirculation Gyres*

HEATHER E. DEESE, LARRY J. PRATT, AND KARL R. HELFRICH

Woods Hole Oceanographic Institution, Woods Hole, Massachusetts

(Manuscript received 25 January 2001, in final form 8 November 2001)

ABSTRACT

Chaotic advection is suggested as a possible mechanism for fluid exchange and mixing among a western boundary current and subbasin recirculation gyres. Applications include the North Atlantic Deep Western Boundary Current and its adjacent mesoscale recirculation gyres. Visualization and quantification of certain aspects of chaotic advection in a laboratory analog are described. Depending on the strength of the forcing, recirculating fluid offshore of the western boundary layer may be contained in a single gyre (not favorable for chaotic advection) or twin gyre with a "figure-eight" geometry (favorable for chaotic advection). When time dependence is imposed on these steady flows by varying the forcing periodically, the resulting fluid exchange, stirring, and mixing is most dramatic in the case of the twin gyre. A template for these processes can be formed by highlighting certain material contours (invariant manifolds) using dye and other techniques. These objects can be used to identify blobs of fluid (turnstile lobes) that are carried into and out of the gyres. The associated transports and flushing times can be estimated. The preferential stirring and mixing in the twin-gyre case is quantified by calculating the effective diffusivity of the flow field based on snapshots of the dye fields at longer times. The experiment suggests how tracers in a western boundary current might be transported into and out of neighboring recirculations and where regions of strong zonal or meridional transport might occur.

1. Introduction

Western boundary currents exchange mass, tracers, and dynamical properties with subbasin-scale recirculations. Observations from the deep North Atlantic have revealed the presence of numerous mesoscale recirculations along the offshore flank of the Deep Western Boundary Current (DWBC). Examples include mesoscale gyres in the Labrador Sea (Lavender et al. 2000, hereafter LRO) near the Gulf Stream undercrossing (Hogg 1992; Bower and Hunt 2000a,b), to the northeast of the Bahamas (Lee et al. 1996; Leaman and Vertes 1996; Johns et al. 1997), and in the Guiana Basin (McCartney 1992; Friedrichs and Hall 1993). Schmitz and McCartney (1993) summarize some of these features along with deep basin-scale gyres. Fine (1995) has shown that tracer-derived ages for the DWBC water are an order of magnitude older than the direct transit time from the source regions based on directly observed velocities in the core of the flow. [Tracer derived velocities

are on the order of 1 cm s^{-1} , while mean observed velocities are on the order of $5\text{--}10 \text{ cm s}^{-1}$ (e.g., Watts 1991).] The discrepancy could be due to the fact that DWBC water is temporarily captured in recirculations during its southward transit (Bower and Hunt 2000a) or that the water adjacent to the DWBC is not tracer-free (Pickart et al. 1989; Rhein 1994). There are also many well-known surface gyres, such as the Great Whirl, the Alboran Gyre, and the Gulf Stream inertial recirculations, that coexist and interact with surface boundary currents.

Tracers, floats, geostrophic calculations, and current meter velocities have been used to construct rough maps of the features mentioned above. An example from the North Atlantic DWBC appears in Fig. 1 (after Johns et al. 1997), which shows the time-average streamline field for the deep flow in the vicinity of Abaco Island. The figure suggests twin gyres just offshore of the main southward flow. (Note, however, that this feature is based largely on geostrophic calculations subject to reference velocity uncertainties.) An annual DWBC transport cycle and 30–150-day onshore/offshore excursions of the DWBC have been detected (Lee et al. 1996), showing that this region is quite time dependent. A substantially more complicated group of deep recirculations in the Labrador Sea has been inferred by LRO using deep and intermediate float data. The dynamical factors leading to the formation of deep gyres are unknown,

* Woods Hole Oceanographic Institution Contribution Number 10450.

Corresponding author address: Larry Pratt, Woods Hole Oceanographic Institution, Mail Stop 21, 360 Woods Hole Rd., Woods Hole, MA 02543.
E-mail: lpratt@whoi.edu

but a number of influences including topographic steering, inertial effects, and interactions with shallower layers are possible. Thompson (1995) and references therein discuss some of these processes within the context of numerical models.

The focus of this work is not on the dynamics of recirculations but rather on a mechanism for exchange and mixing among recirculations and boundary currents. Such exchange is sometimes modeled as a diffusion process (Pickart and Hogg 1989) in which tracers cross the closed boundaries of steady recirculations. This view of tracer spreading is consistent with conventional ideas regarding classical turbulence, in which small-scale eddies give rise to coarse grain diffusion of passive tracers. However the observed geometry of deep recirculations and the presence of time dependence suggest that chaotic advection could also be a factor. This process, which is thought to account for the transport of chemical species in the stratospheric polar vortex (Haynes 1999), involves advective mass exchange between regions of fundamentally different motion due to time dependence. The mass that is exchanged typically undergoes rapid filamentation, a process that leads to intensification of property gradients and is therefore a catalyst for irreversible mixing through diffusion or subgrid-scale turbulence. Chaotic advection is generally associated with the occurrence of strong hyperbolicity (stretching and contraction about a certain parcel trajectory). The tendency of closely spaced pairs of parcels to separate from each other exponentially in time as they pass such a trajectory is a fundamental characteristic of chaotic motion.

In a steady flow, a hyperbolic trajectory is simply a saddle-type stagnation point. Such points occur in the Abaco recirculation system, approximately at the locations marked H in Fig. 1. An idealized sketch of a similar recirculation pair (Fig. 2) indicates a single hyperbolic point at the self-intersection of the figure-eight separatrix. Recirculations need not have such points, as shown for the single gyre sketched in Fig. 2b. If a time-dependent perturbation is imposed, chaotic advection might be expected to occur more readily and with greater effect in the twin-gyre case (or in other geometries having saddle-type stagnation points) than in the single-gyre case.

The above remarks suggest that fluid exchange and mixing along the DWBC may depend upon the underlying geometry of the adjacent recirculations. In particular, more extensive and intense mixing would seem to be favored by geometries containing strong hyperbolicity. The purpose of our work is to verify this conjecture by visualizing and quantifying fluid stirring and mixing in a laboratory model of a western boundary layer with neighboring single- or twin-recirculation gyres. In cases where fluid exchange occurs, we would like to determine the pathways by which fluid enters and leaves the gyre(s). Visualization of the flow is achieved using dye and particle imaging, and the mixing is quantified using

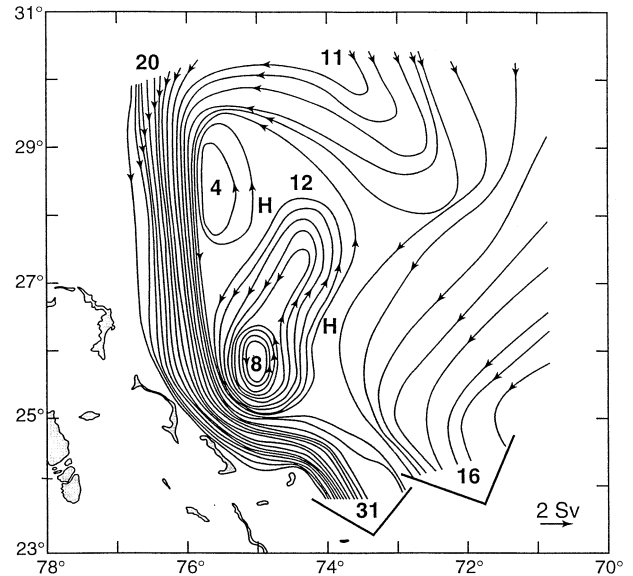


FIG. 1. Approximate streamlines of the deep flow below potential temperature 6°C , or about 1000-m depth. The contour interval is 2 Sverdrup ($\text{Sv} \equiv 10^6 \text{ m}^3 \text{ s}^{-1}$). Possible locations of hyperbolic trajectories are labeled "H". Adopted with permission from a figure of Johns et al. (1997).

effective diffusivity (Nakamura 1996) measured from dye distributions. The laboratory model is barotropic and the dynamics therefore differ somewhat from those governing abyssal flows. However, chaotic advection is a generic mechanism depending largely on the underlying geometry of the flow. Differences between stirring patterns observed in the laboratory model may be helpful in understanding exchanges between boundary currents and subbasin recirculations in general and in suggesting strategies for observing exchange processes in the field. A moderate volume of literature on chaotic advection has developed over the past 15 yr, and some of our ultimate conclusions could have been anticipated on the basis of this work. However, laboratory models of chaotic advection are quite rare and the particular application to western boundary layer recirculations is novel.

Section 2 reviews some of the basic objects and terminology used in connection with chaotic advection, including hyperbolic trajectories and their stable and unstable manifolds. Such objects can be used to construct a template for exchange and mixing among distinct regions of a flow field. Section 3 describes the laboratory apparatus, experiment, and dimensionless parameters. (Briefly, the flow is set up in a sliced cylinder with a differential lid rotation. The steady-state flow consists of a Sverdrup interior, a western boundary layer, and a single- or twin-recirculation gyre. The geometry of the gyre is determined by the strength of inertia, ultimately controlled by the differential lid rotation. Time dependence is induced by periodically varying the rate of differential rotation.) Section 4 is concerned

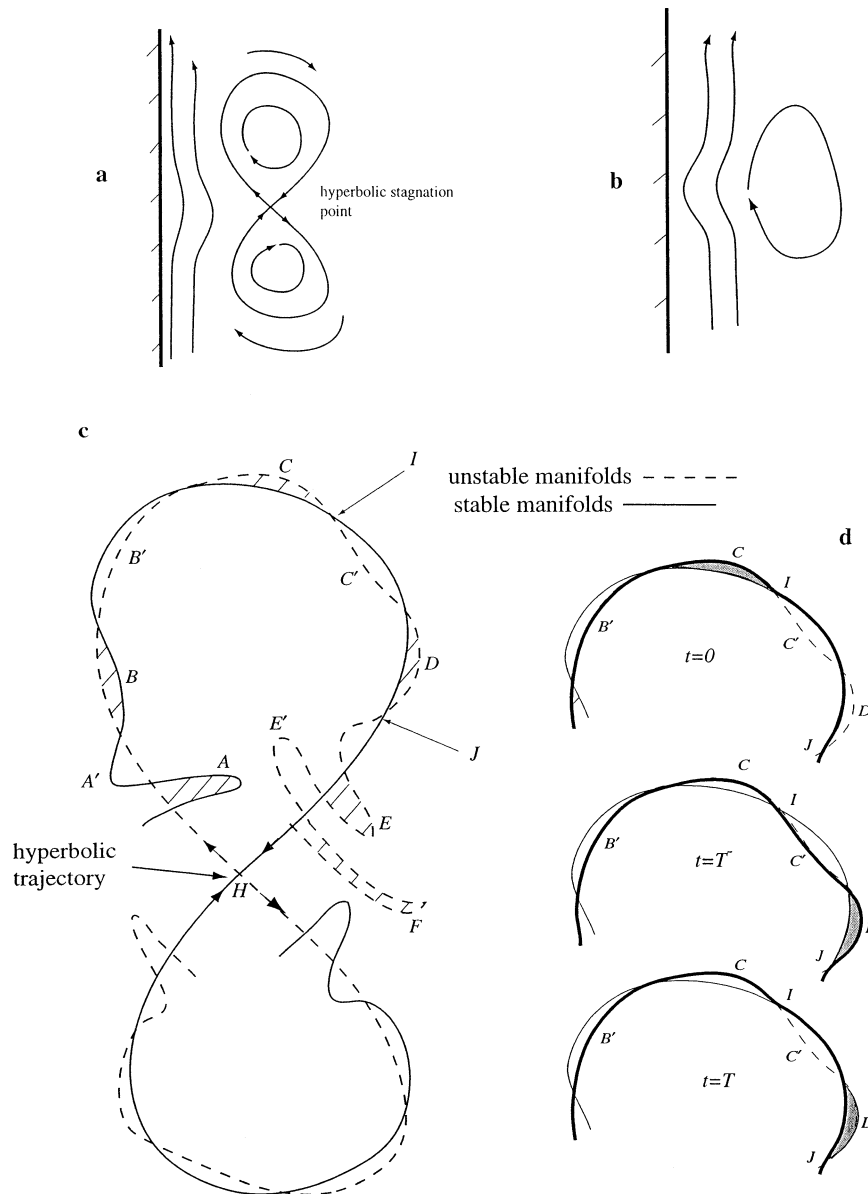


FIG. 2. (a) and (b) Show steady streamline patterns for hypothetical twin- and single-gyre recirculations near a western boundary current. (c) The stable and unstable manifolds of the central hyperbolic trajectory for the time-dependent twin gyre. Stable manifolds are solid and unstable manifolds are dashed. The letters A, B, etc. denote material lobes of fluid that are being transported out of the northern gyre. A', B', etc. denote lobes containing fluid that is being transported into the northern gyre. (d) The recirculation boundary (thick solid line) formed by joining sections of the (dashed) unstable and (thin solid) stable manifolds. This boundary evolves as a material contour from $t = 0$ to $t = T^-$ at which time it is redefined ($t = T$).

mainly with visualization of the stirring and exchange process using dye. The dye patterns show profound differences between the single- and twin-gyre cases and suggest where and how, in the twin-gyre case, recirculating fluid is exchanged and mixed with surrounding fluid. Section 5 quantifies the mixing process in terms of effective diffusivity, a bulk measure of the enhancement of diffusion by advective filamentation of dyed

blobs. Section 6 contains a summary and discussion of ramifications of the work.

2. Hyperbolic trajectories, manifolds, and lobe dynamics

In order to describe the transport and stirring processes associated with chaotic advection, it is helpful

to use certain Lagrangian objects including hyperbolic trajectories, stable and unstable manifolds, and turnstile lobes. We use these material objects to construct a template for exchange processes due to the time dependence of the flow and to measure the associated volume fluxes. The following is a quantitative review; more complete and formal discussions can be found in Rom-Kedar and Wiggins (1990) and Wiggins (1992). It is generally assumed that the flow in question is 2D and horizontally nondivergent, or at least so to a first approximation.

We have previously referred to Figs. 2a,b depicting steady twin- and single-gyre recirculations. Note that the saddle-type fixed point in Fig. 2a has stable and unstable directions (as indicated by the arrows) corresponding to the directions of contraction and stretching. The streamlines extending away from the saddle point along these directions form the figure-eight separatrix that defines the boundaries of the recirculations. If these hypothetical flows are perturbed in a time-dependent manner, and if the perturbation is not too large or rapid, then generalizations of the stagnation points will exist. The generalization of the saddle-type fixed point in Fig. 2a is a distinguished hyperbolic trajectory (DHT), a fluid parcel path having stable and unstable directions (i.e., directions of strong contraction and stretching) for all time. The location of this parcel and the orientation of the stable and unstable directions will vary with time, but the trajectory will remain in the vicinity of the steady saddle point.

If dye is continuously introduced at the (moving) location of the DHT, it will leave the area along the two unstable directions forming two material contours, the *unstable manifolds*. Another set of material contours consists of fluid that is attracted to the DHT and approaches it along the stable directions asymptotically in time. In numerical simulations, these *stable manifolds* can be found by introducing “dye” at the DHT and running time backward. Hypothetical stable and unstable manifolds for a DHT resulting from the figure-eight geometry are sketched in Fig. 2c. The solid and dashed curves are the stable and unstable manifolds, respectively, at a particular time.¹ Unlike Fig. 2a, where the stable and unstable manifolds correspond to the same material curves, the manifolds for the unsteady case are distinct curves that often tangle about each other. The tangle is evidence that chaotic Lagrangian motion exists in the vicinity of the intersecting manifolds. A fundamental characteristic of this motion is that nearby fluid parcels separate from each other exponentially in time, implying rapid stirring of the fluid. Even in systems where chaos cannot formally be defined, the presence of tangled manifolds still implies exponential separation of fluid parcels over finite times.

The exchange and stirring mechanism in the unsteady flow is revealed by considering a lobe of fluid (marked *A* in Fig. 2c) trapped between the stable and unstable manifolds. Since the manifolds are material curves the fluid in such a lobe must remain trapped between the manifolds and must preserve area as the flow evolves. In general, the lobe will follow the direction of the cyclonic swirling flow around the recirculation and will, after a certain time interval, lie at cross-hatched position *B*, then *C*, and so on. Since Fig. 2c shows the manifolds at a particular time, the lobes at *B*, *C*, *D*, etc. do not necessarily depict the result of the evolution of the lobe at *A*. However, the reader may be able to imagine the evolution as the lobe moves around the periphery of the recirculation from *A* to something like *F*, a process that has two profound results. First, the fluid at *A*, initially inside of the recirculation, has clearly moved outside of the recirculation at *F*. (At the same time, fluid outside moves inside by following something like the cross-hatched lobes *A'*, *B'*, etc.) Second, the evolving lobe is stretched into a filament, such as the one at *F*. Fluid is thereby stretched and folded as it is drawn into and out of the recirculation, a process that increases the spatial gradients of any materially conserved properties. The exchange process thus acts as a catalyst for mixing by sharpening gradients so that diffusion can act more rapidly. A similar mechanism can generally be expected to act in connection with the southern gyre.

If the Eulerian time dependence is periodic with period *T*, as is nearly the case in our laboratory experiment, the shapes of the manifolds recur on period *T*. Lobe *A* then evolves *exactly* into lobe *B*, then *C*, and so on. Although this progression may not always be in sequence (e.g., lobe *A* may map to *C* and then *E*, while *B* maps to *D* and then *F*), sequential mapping is observed in the experiment. In this case, *A*, *B*, *C*, etc., must have the same area. As we will demonstrate below, *A* and *A'* (and therefore *B'*, *C'*, etc.) must also have equal areas.

The above discussion has tacitly assumed that the velocity field is known over infinite time and that the hyperbolic trajectories persist over that time. If the time-dependent motions are violent enough, hyperbolicity can become intermittent; a situation that apparently does not arise in the laboratory experiment described below. A more immediate complication is that the velocity field is known only over finite time, as is the case in all laboratory, numerical, or field experiments with non-periodic time dependence. Finite time duration leads to uncertainty in defining DHTs; a continuous group of nearby trajectories may all exhibit strong hyperbolicity (stretching and contraction) over the time record. In practice, one can usually select a particular hyperbolic trajectory from this group, approximate its stable and unstable manifolds, and perform the same analysis as before. The investigator is simply mapping out convenient material curves that reveal particular Lagrangian structures and transport in the flow field. The reader

¹ Normally, the term “manifold” refers to a *surface* in (x, y, t) space consisting of material that asymptotically approaches or departs from the DHT. The *curves* in Fig. 2c, often referred to as manifolds themselves, are actually time slices through these surfaces.

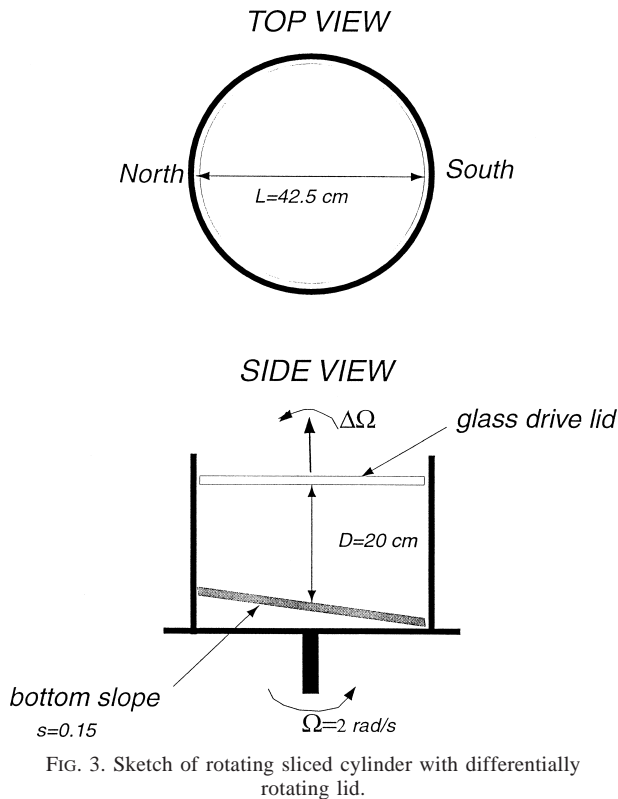


FIG. 3. Sketch of rotating sliced cylinder with differentially rotating lid.

who wishes to wade deeper into this subject is referred to Miller et al. (1997, 2002), Malhotra and Wiggins (1998), Rogerson et al. (1999), and Ide et al. (2001).

Stable and unstable manifolds can be used to define a formal Lagrangian recirculation boundary and to quantify the volume flux across that boundary. In Fig. 2c, for example, a boundary might be defined (at $t = 0$, say) as the curve that begins at the hyperbolic trajectory H and follows the dashed contour extending to the upper left. When the intersection point I with the solid curve is reached, one switches to the solid curve and follows it back to the hyperbolic trajectory. The boundary at $t = 0$ is thus the union of the dashed curve HI and solid curve IH . A subsegment of this boundary is shown as a darkened line in the $t = 0$ frame of Fig. 2d. As time progresses this closed material curve deforms. If the time-dependence is periodic (with period T) however, the shapes of the manifolds themselves recur at $t = T, 2T$, etc. In this case the material intersection point I moves to another intersection, say J , as t progresses from 0 to T . Over the same time period the material boundary evolves into the darkened line in the middle frame of Fig. 2d. At this point it is standard practice to redefine the boundary to coincide with its position at $t = 0$ (lower frame of Fig. 2d). The times immediately before and after boundary redefinition are designated T^- and T . As a result of this redefinition, some of the material inside the gyre now lies outside, and vice versa. Specifically, material in lobe C at $t =$

TABLE 1. Constant dimensional and nondimensional values for laboratory tank.

$L = 42.5$ cm	$\beta = 3$ (ms) $^{-1}$	$\beta = fs/H$
$D = 20$ cm	$\beta^* = 0.3$	$\beta^* = \beta L/f$
$s = 0.15$	$\delta_M = 0.7$ cm	$\delta_M = (v/\beta)^{1/3}$
$\Omega = 2$ rad s $^{-1}$	$\delta_S = 0.5$ cm	$\delta_S = r/\beta = \delta_E f/\beta D$
$f = 2\Omega = 4$ rad s $^{-1}$	$\delta_E = 0.07$ cm	$\delta_E = (v/\Omega)^{1/2}$
$v = 0.01$ cm 2 s $^{-1}$	$E^{1/2} = 0.0035$	$E^{1/2} = \delta_E/D$

0 (shaded in Fig. 2d) has moved to lobe D at $t = T$. Lobe C lies inside the boundary at $t = 0$ but D lies outside the (redefined) boundary at $t = T$. The result is a “chaotic transport” out of the gyre equal to the area of C divided by T . At the same time, material in lobe B' outside the boundary has moved to C' inside. Since the boundary recurs periodically, lobes B' and C (and therefore all other lobes) must have equal area. The swapping of fluid across the boundary of the recirculation has led to the term *turnstile lobes*. Some investigators prefer to think of the boundary as a *fixed* curve defined by the union of the manifolds at $t = 0$, a definition that does not alter the transport value. The movement of fluid across this boundary is continuous rather than discrete in time. However, use of a fixed boundary is less meaningful if the time-dependence is aperiodic.

The boundary of the time-dependent recirculation can be chosen in a variety of ways and this choice determines where fluid enters and leaves the recirculation. If we had picked an intersection point other than I (Figs. 2c or 2d) as the joining point, this would have led to a different definition of the interior of the recirculation and different regions of entry and exit. However, some choices lead to bizarre recirculations bearing little resemblance to the corresponding mean or steady recirculation. The usual practice is to choose such that the resemblance is strong.

3. Lab apparatus and procedure

A barotropic western boundary current and adjacent single or double recirculation gyres can be set up in a rotating “sliced cylinder”: a cylindrical laboratory tank with a sloping bottom (Fig. 3). The relevant dimensional and nondimensional parameters appear in Tables 1 and 2. The discussion below and the appendix describe the general procedures used but spares the reader many of the technical details. The latter are thoroughly covered in Deese (2001), available upon request to Dr. Pratt.

The tank is 42.5 cm in diameter, has a mean depth of 20 cm, and is fitted with a bottom of slope $s = 0.15$. The actual depth therefore varies from 16.8 to 23.2 cm. The tank rotates at a fixed rate $\Omega = 2$ rad s $^{-1}$, leading to a topographic beta $\beta = fs/H = 3$ (ms) $^{-1}$. The circulation is driven by a lid that rotates at a differential rate $\Delta\Omega < 0$, producing a uniform, anticyclonic surface stress curl. The surface stress results in the formation of an Ekman layer of thickness $\delta_E \equiv (v/\Omega)^{1/2} = 0.07$

TABLE 2. Variable dimensional and nondimensional values for lab tank.

$\Delta\Omega(1 \text{ s}^{-1})$	0.0076	0.0173	0.0480	0.2777 ^a
$\epsilon = \frac{\Delta\Omega}{\Omega}$ (nd)	0.0038	0.0087	0.0240	0.0139
$\delta = \frac{\delta_1}{\delta_M} = 8.1 \sqrt{\frac{\Delta\Omega}{\Omega}}$ (nd)	0.50	0.75	1.25	3.00
$w_E = \Delta\Omega \cdot \delta_E$ (cm s ⁻¹)	0.00053	0.00120	0.00336	0.0194
$U_S = w_E/s$ (cm s ⁻¹)	0.0035	0.008	0.022	0.129
$U_{wbc} = U_S \cdot L/\delta_{wbc}$ ^b (cm s ⁻¹)	0.047	0.107	0.293	1.72
$U_S/\beta L^2$	7.3×10^{-5}	1.7×10^{-4}	4.6×10^{-4}	2.7×10^{-3}
$Re = UL/\nu$	14	32	88	516
$Ro = U_S/fL$	2.2×10^{-5}	5.0×10^{-5}	1.4×10^{-4}	8.1×10^{-4}
$Ro = \Delta\Omega/2\Omega$	0.0019	0.0044	0.012	0.070
$\epsilon/E^{1/2}$	1.08	2.47	6.86	39.71

^a The flows for this setting were unsteady and were not used as a basis for any experimental runs.

^b Based on approximate observed value of western boundary layer thickness δ_{wbc} .

cm (ν being the kinematic viscosity of water) with a uniform vertical velocity $w_E = \Delta\Omega\delta_E < 0$ at its base. Away from the dynamical western boundary this downwelling gives rise to a southward Sverdrup transport with typical meridional velocity $U_S = w_E/s$. The Sverdrup character of the regime is confirmed by the small values of Rossby number and $U_S/\beta L^2$, both $O(10^{-4})$.

Three types of boundary layers, the Stommel and Munk frictional western boundary layers and the inertial boundary layer, all come into play at the dynamical western boundary. The corresponding boundary layer thicknesses are given by

$$\delta_M = \left(\frac{\nu}{\beta}\right)^{1/3}, \quad \delta_S = \frac{\delta_E f}{D\beta}, \quad \text{and} \quad \delta_I = \left(\frac{U_S}{\beta}\right)^{1/2}.$$

As it turns out, δ_M (at 0.7 cm) and δ_S (at 0.5 cm) are quite close and constant in these experiments. We therefore treat the ratio $\delta = \delta_I/\delta_M = 8.1(\Delta\Omega/\Omega)^{1/2}$ as the primary indicator of nonlinearity near the western boundary layer. Our experiments are restricted to $\delta \leq 1.4$, for which the flow is steady, or very nearly so, in the presence of steady lid rotation. Time variation about the steady states is imposed by varying the lid rotation according to

$$\Delta\Omega(T) = \Delta\Omega_o[1 + A_{osc} \sin(2\pi t/T_{osc})].$$

Three methods are used for visualizing and measuring the horizontal circulation. The first two involve the tracking of neutrally buoyant plastic particles suspended in the tank and illuminated by a horizontal sheet of light generated by an argon ion laser. Streak images showing the trajectories of the particles over short time intervals are made from digital video recordings of the flow. Direct velocity measurements are also made in a limited area using particle image velocimetry (PIV; Raffel et al. 1998). This process involves calculation of the velocity field implied by the difference in particle locations between two video frames taken in close succession. The camera and analysis algorithm allows for measurement of velocities with a spatial resolution of 1 cm. As

described in the appendix, this resolution is insufficient to perform a lobe analysis that adds significantly to what can be done with dye. Instead, PIV is used to make accurate velocity measurements over a limited area of the flow field in order to quantify the time dependence of the flow. The third visualization technique involves the introduction of dye into the flow using a needle. Dye patterns are illuminated from below and recorded from above using a video camera. The images are later digitized. The appendix contains further technical information regarding the particle and dye techniques.

For cases of steady lid forcing, the (nearly) steady flows² observed agree with those found in laboratory experiments with similar forcing and geometry (Pedlosky and Greenspan 1967; Beardsley 1969; Griffiths and Kiss 1999). With δ less than about 1.1 the nearly steady flow field in western reaches of the tank consists of a western boundary layer and a single recirculation gyre. Within the range $1.1 < \delta < 1.4$, the recirculation splits into twin gyres.³ Both steady regimes are revealed by a sequence of streak images (Fig. 4) for the western two-thirds of the tank. In this and other photos of the circulation, the lower boundary is the western boundary and north is to the left. Note that a shadow obscures a portion of the western boundary layer. The single-gyre geometry occurs for $\delta = 1.00$ (Fig. 4a). If δ is increased past about 1.1 (Fig. 4b) the gyre splits forming the figure-eight twin gyre shown in Figs. 4c,d ($\delta = 1.25$ and 1.4). [The hyperbolic stagnation point is marked by an isolated white dot to the lower right of the northern (left-hand) recirculation in Fig. 4c.] The twin-gyre regime persists until $\delta \cong 1.40$ beyond which a single gyre reappears and natural unsteadiness increases, the latter a possible result of the interior instability discussed by Meacham and Berloff (1997). The remainder of discussion is confined to the single ($\delta < 1.1$) and twin (1.1

² Griffiths and Kiss (1999) find very slow time dependence in a similar experiment, even for values of $\delta < 1$.

³ In a similar experiment, Beardsley (1969) notes twin gyre formation at $\delta = 0.75$.

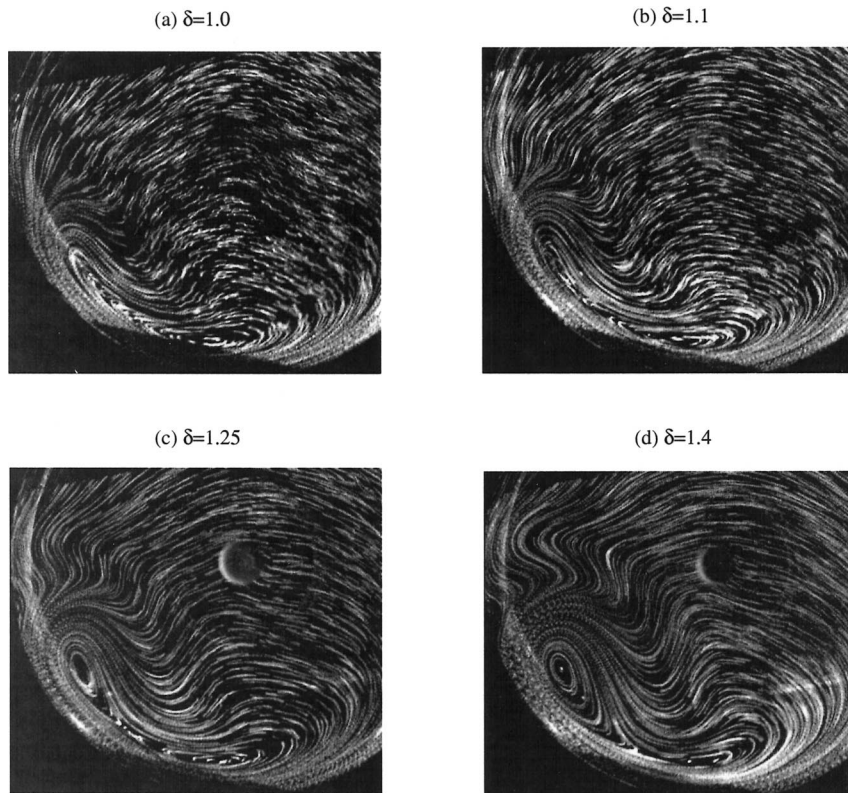


FIG. 4. Streak images showing nearly steady flow for various δ . North is to the left and west is downward.

$< \delta < 1.4$) gyres and a comparison of stirring and mixing between these geometries under time-dependent perturbations forced by the lid.

4. Visualization of stirring, mixing, unstable manifolds, and turnstile lobes

Different Lagrangian aspects of the flow can be visualized by injecting dye into the tank through a needle. The needle is orientated radially, as shown in Fig. 5, and can be extended or retracted allowing injection into the southern recirculation interior or the western boundary layer. The approximate boundary of the steady, twin recirculation gyre (with $\delta = 1.25$) can be visualized by positioning the tip of the needle very close to the western edge of the southern gyre. The resulting dye streak is shown 9 and 21 min after injection is started (Fig. 5). The dye initially moves northward until the hyperbolic stagnation point is reached. There it splits into two streaks, one of which traces the western edge of the northern gyre and one of which traces the eastern edge of the southern gyre (Fig. 5a). Later the remaining boundaries of the gyres have been completely traced, revealing the figure-eight separatrix (Fig. 5b). The wispi-ness of the dye is thought to be due to double diffusion between the salty ambient water and the food color dye. (Salt was added to match the density of the dye.) Note

that the southern gyre is thinner and less distinct than the northern gyre, a feature that has led us to focus further investigation on the northern gyre.

In order to force the simplest possible time dependence, the period T_{osc} of lid oscillation was chosen to match the period $2\pi/\Delta\Omega$ of differential lid rotation (20–131 s). This choice insured that any periodic disturbances introduced by imperfections in the lid would simply add to the periodic disturbance forced by the oscillating surface stress. To get a measure of the actual time dependence, we calculated the power spectrum of kinetic energy (Fig. 6) at a location near the eastern edge of the northern member of the twin gyre for $\delta = 1.25$ and $A_{\text{osc}} = 0.15$. The velocity at this location was obtained from PIV measurements over a time span of $9 T_{\text{osc}}$. The peak near 0.01 Hz corresponds to motions at the forcing frequency and lies an order of magnitude higher in power density than all other peaks save the one between 0.3 and 0.35 Hz. The latter corresponds to the 3.14-s rotation period of the tank and is thought to be caused by variations of light intensity at this period due to imperfections in the rotating fiber optic coupling.⁴

⁴ The PIV algorithm computes fluid velocities by comparing patterns set up by (light) beads and (dark) fluid at slightly different times. The algorithm works best if the background light intensity is steady and uniform. If the light is not spatially uniform, temporal

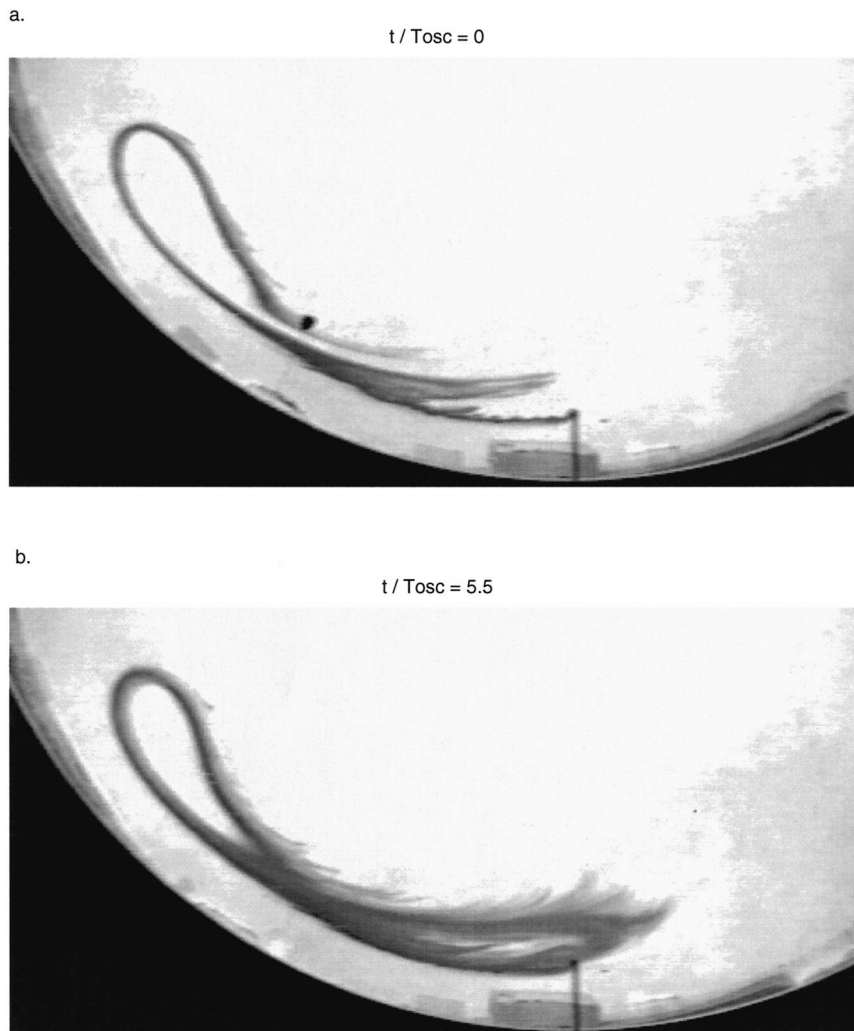


FIG. 5. Dye intrusion tracing the edge of the steady figure-eight gyre. The dimensionless times $t/T_{osc} = 0$ and 5.5 correspond to 9 and 21 min after injection is begun. North is to the left and west is downward. The dye needle is shown as a thin line protruding through the western boundary.

There may also be unsteadiness in the flow at this high frequency due to irregularities in the drive train, but no obvious indication of this was detected in the dye visualizations described below.

As expected, the time dependence introduces considerably more stirring in the twin-gyre case than the single-gyre case. One basis for comparison is the dye patterns produced after many forcing periods (Fig. 7, with $A_{osc} = 0.05$). The three images show two single-gyre cases ($\delta = 0.75$ and 1.00) and one twin-gyre case ($\delta = 1.25$). Dye was injected for 23 min in what was judged to be the interior of the single recirculation or, in the final case, the interior of the southern gyre. The images were recorded 54 min after injection was started leading

to very diffuse distributions. In the single-gyre cases (top two frames) the dye remains confined to the interior of the recirculation, even though the flow is unsteady. The twin-gyre case (lower frame) produces a more extensive pattern of folds and filaments that extend eastward away from the gyres.

We believe that the extended strands of dye that appear in Fig. 7c result from stretching and folding associated with a distinguished hyperbolic trajectory (DHT) and its stable and unstable manifolds. Earlier, we sketched these processes by showing the evolution of lobes of fluid trapped between stable and unstable manifolds in a hypothetical flow (Fig. 2). Very similar objects can be seen in images taken sooner after introduction of the dye. The sequence in Fig. 8 shows the evolution of the dye contour over two periods of the lid oscillation for the twin gyre with $\delta = 1.25$, $A_{osc} = 0.05$, and $T_{osc} = 131$ s. As before, dye is in-

variations in intensity can induce apparent pattern shifts, causing the algorithm to detect false velocities.

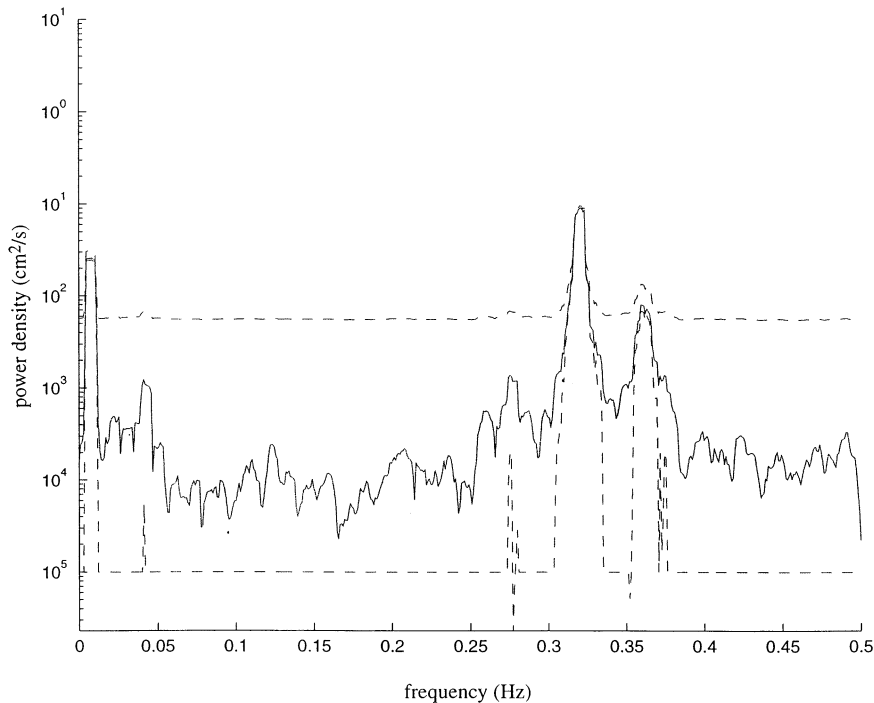


FIG. 6. Power spectrum of fluid speed calculated at a location in the eastern portion of the northern recirculation. Dashed lines indicate 95% confidence limits.

jected very close to the western boundary of the southern gyre, just upstream of the suspected hyperbolic trajectory. The hope was that some of the dye would find its way into the region around the hyperbolic trajectory and, from there, split and follow the unstable manifolds. About three cycles after injection is begun (Fig. 8a, $t/T_{osc} = 0$), the initial dye line has moved along the western edge of the southern gyre and split at the hyperbolic trajectory, forming a northward (to the left) moving strand that encircles the northern gyre and a southern strand that moves along the east side of the southern gyre. The northern strand does not close to form the northern boundary of the figure-eight, as it does in the steady case. If fact, the tip of the strand can be seen in Fig. 8b far to the right of the DHT. Beginning at this tip and following the strand backward (to the left), one encounters several sharp turns or meanders. The first sharp turn is part of a narrow wedge of fluid that is beginning to wrap around the inside edge of the northern gyre. As time progresses, additional meanders form in the strand at the eastern edge of the northern gyre (Fig. 8c). These meanders steepen and fold into wedges or filaments (Fig. 8g) that are alternately pulled into or drift southward of the northern gyre. The filaments pulled into the northern gyre spiral anticyclonically about the inside edge. The southward filaments continue to drift southward along the eastern side of the southern gyre. After nearly two cycles ($t/T_{osc} = 1.8$) of lid oscillation,

we see that two additional southward filaments have formed. Precise measurements indicate that T_{osc} is indeed the time interval between passage of the edges of consecutive filaments across a fixed location. All of these features are characteristic of the unstable manifold for the northern gyre of the hypothetical flow (Fig. 2c).

The above picture suggests an exchange process between the northern gyre and surrounding fluid. A quantitative description of this transport could be made by locating the stable manifolds of the DHT, allowing turnstile lobes to be identified. Although stable manifolds can be calculated in numerical simulations by running time backward, no simple method for finding a stable manifold in a laboratory experiment exists. In principle, one could store PIV velocity information on a horizontal grid over a full period of oscillation and, with this complete velocity record, do a backward time simulation. Instead, we have attempted to identify turnstile lobes by approximating the position of the stable manifold extending immediately northeastward from the hyperbolic trajectory. That is, we approximate something analogous to the solid line in Fig. 2c extending a short distance to the upper right of the DHT. The approximation consists of a short line segment extending northeastward from the suspected position of the hyperbolic trajectory at a given time and in a direction that bisects the filaments so as to give equal area on either side of the line. As described in section

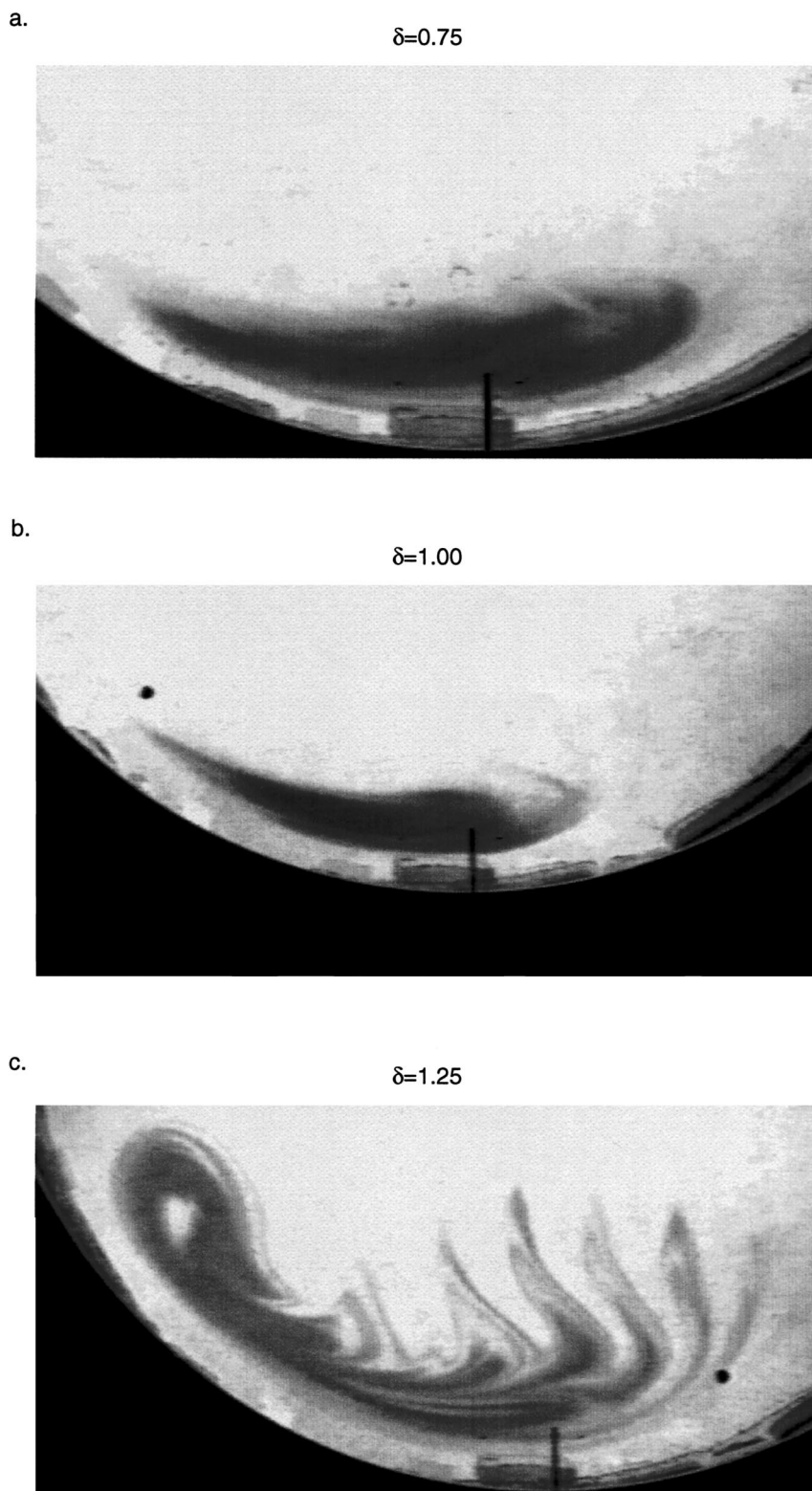


FIG. 7. Dye patches 54 min after injection for unsteady flows ($A_{\text{osc}} = 0.05$) with single-gyre geometry ($\delta = 0.75, 1.00$) and twin-gyre geometry $\delta = 1.25$. North is to the left and west is downward.

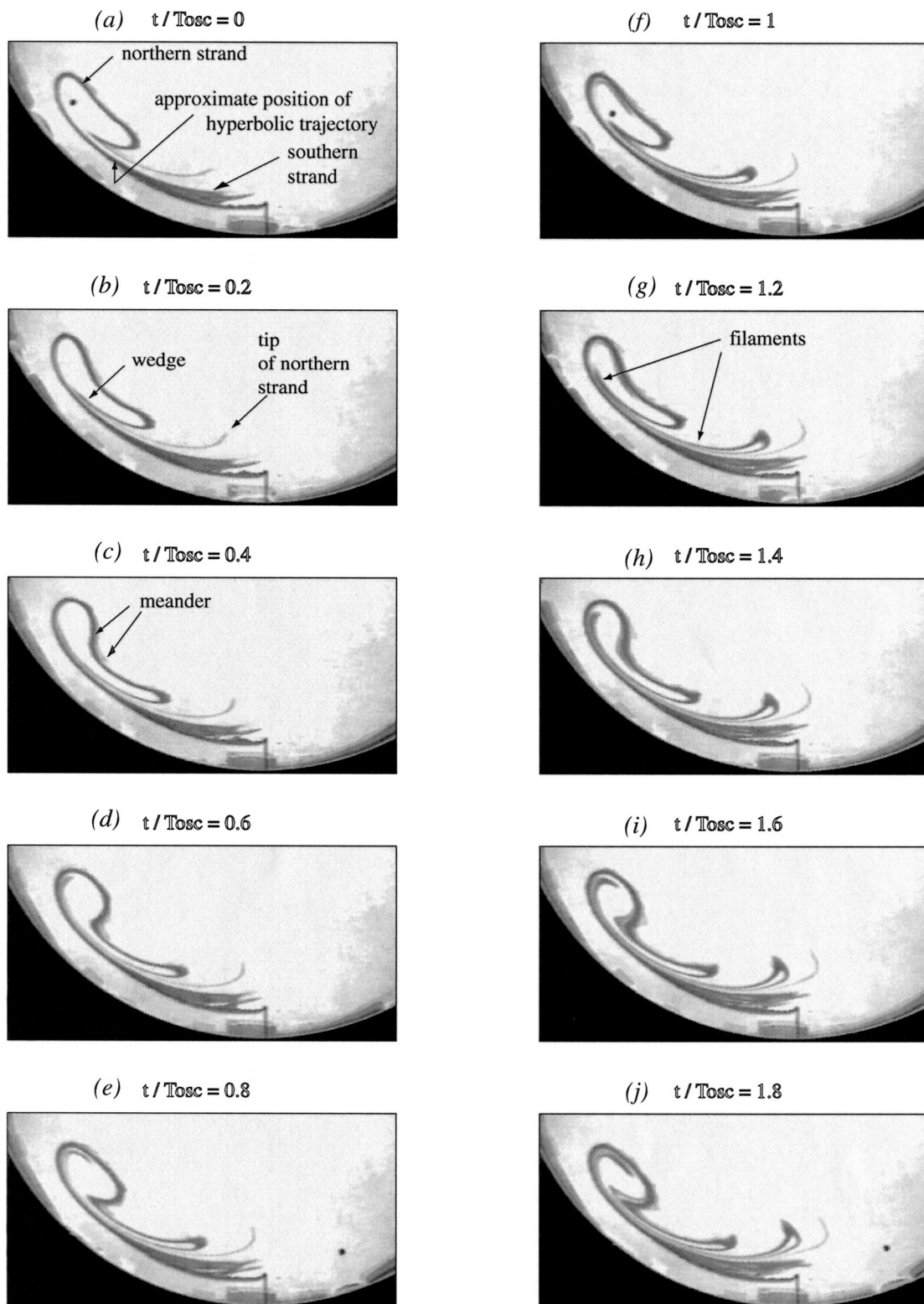


FIG. 8. Evolution of dye lines over two forcing cycles for $\delta = 1.25$ and $A_{osc} = 0.05$. North is to the left and west is downward.

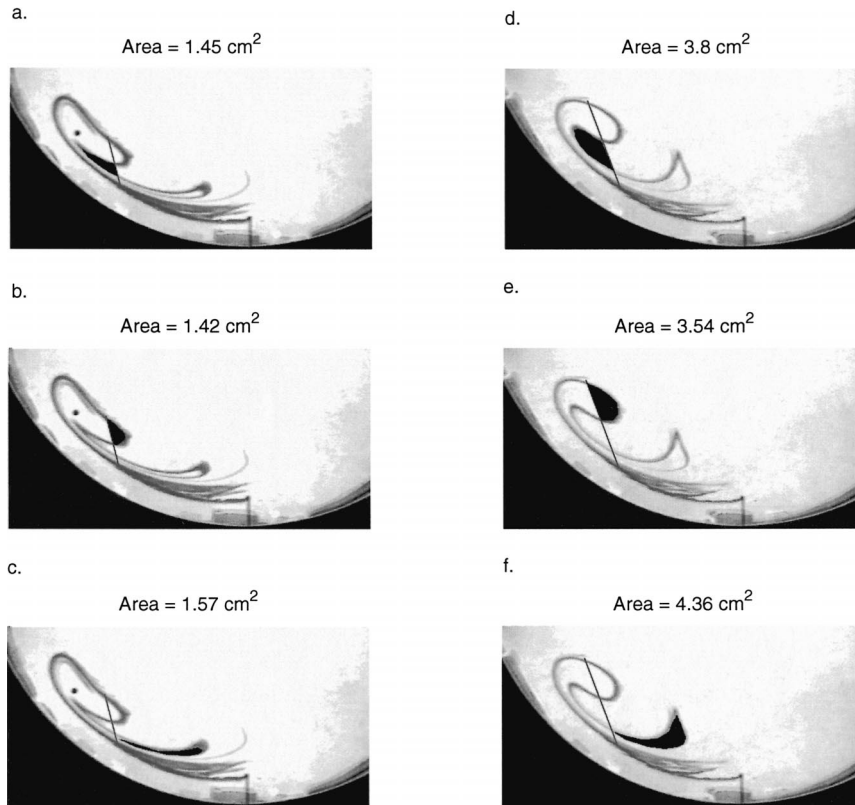


FIG. 9. Dye lines similar to those shown in Fig. 8 with an approximation (the straight line segment) to the stable manifold for the northern gyre. The darkened patches are approximations of turnstile lobes; their areas are labeled above each frame: (a)–(c) $\delta = 1.25$ and $A_{osc} = 0.05$, (d)–(f) $\delta = 1.25$ and $A_{osc} = 0.15$. North is to the left.

2, the requirement of equal lobe areas, a consequence of mass conservation, holds as long as the horizontal velocity is nondivergent, the time-dependence is periodic, and only a single lobe enters the recirculation during each period.⁵ In the experiment the first two conditions hold to within a good approximation whereas the third holds exactly.

We have applied the above method in order to approximate a short section of the stable manifold for the Fig. 8 flow. The result is a hand-drawn line segment extending from the position of the DHT northeastward (Figs. 9a–c). It intersects the wavy unstable manifold such that the first three identifiable lobes have approximately equal areas. Each of the three lobes is darkened individually in Figs. 9a–c and their areas are given. When A_{osc} is increased from 0.05 to 0.15 the corresponding lobes become larger (Figs. 9d–f). Naturally,

⁵ In some cases, a requirement of equal lobe volume is appropriate. For example, if the bottom slope in the tank was large enough to cause significant depth differences on the scale of the recirculation, and if the flow obeyed inviscid shallow-water dynamics [implying $\partial u/\partial x + \partial v/\partial y \neq 0$ but $\partial u/\partial z = \partial v/\partial z = 0$], then the manifolds would be independent of depth and the lobes would have unequal horizontal area but equal volume. The presence of friction boundary layers at the top or bottom might invalidate this equality.

there are uncertainties involved with this exercise. The position of the hyperbolic trajectory must be guessed and the use of a straight, rather than curved line, means that the three lobe areas can almost never be exactly equal. Nevertheless, the construction allows one to visualize approximations to the real lobes. The darkened lobe in frame (a) contains fluid entering the recirculation while those of (b) and (c) contain fluid that is leaving. Likewise, the frame (d) darkened lobe contains entering fluid while the frames (e) and (f) darkened lobes contain departing fluid.

The flux or “chaotic transport” F of fluid into (or out of) the northern gyre can be calculated by dividing the area of any single lobe by the period T_{osc} (section 2). We have carried out this calculation using the average of the lobe areas shown in Figs. 9a–c (or 9d–f) as an estimate of the actual lobe area. From the resulting F , a flushing time for the northern gyre can be estimated by defining the gyre boundary as the union of the line segment in Fig. 9 with the portion of the unstable manifold extending from the northern end of the line segment counterclockwise back to the other end of the line. (The resulting gyre area A_g is approximately the same as in the steady case.) Measuring the enclosed area gives flushing times $A_g/F \cong 9T_{osc}$ for the case of weaker time

dependence ($A_{\text{osc}} = 0.05$) and about $3T_{\text{osc}}$ for $A_{\text{osc}} = 0.15$. Interpretation of flushing is complicated by the fact that the lobes do not appear to fill the entire area inside the recirculation, as suggested by the clear area in the center of the northern gyre in Fig. 7c. Thus the actual area being flushed is probably smaller than A_g .

Anthropogenic ocean tracers tend to be introduced at the source region of a deep western boundary current and are thought to be transported from the boundary current into the recirculations. The fate of a tracer introduced in the western boundary layer of the laboratory flow is shown in Fig. 10a. Dye is injected just outside of the southern gyre for a time-dependent case with $\delta = 1.25$, $A_{\text{osc}} = 0.05$. The dye is carried northward and eventually around the northern and eastern edges of the northern gyre. Some of this dye is transported into and later expelled from the northern gyre by a process resembling the turnstile mechanism. Evidence for the latter exists in the form of alternating dark and light filaments that pass a fixed location at exactly the forcing period. However, the dye has not been introduced so as to map out the manifolds and the filaments shown are therefore not exactly turnstile lobes. Some of the material expelled from the recirculation penetrates far eastward into the Sverdrup interior.

Tracer injected just *inside* the western edge of the southern gyre evolves in a qualitatively similar way (Fig. 10b). Some of the dye makes its way into the northern gyre and escapes in filaments similar to the above. Only when dye is injected into the very center of the southern gyre does it remain largely confined there (Fig. 10c). This confinement is an indication that the center of the gyre is protected by a barrier penetrable only by molecular diffusion. Evidence for a barrier in the interior of the northern gyre can be seen in the form of dye-free centers in Figs. 10a and 10b (also see Figs. 7c and 8).

5. Effective diffusivity calculations

a. Background

Although the visual evidence is that the figure-eight geometry of the twin gyre leads to considerably more stirring and mixing under time dependence than the single-gyre geometry, this remains to be quantified. To do so, we employ the theory of effective diffusivity (Nakamura 1996; Winters and D'Asaro 1996), which provides for bulk quantification of the catalytic effect of stirring in producing molecular (or subgrid scale) property exchanges. Stirring is indicated by the geometric complexity of the flow resulting from the contortion of tracer contours due to advection. The product of the analysis is an "effective" diffusion coefficient κ_{eff} that depends on both the contortion in the tracer field and the molecular diffusivity.

The formal theory involves definition of a new variable $A(C, t)$, the area enclosed by a given contour C

of passive tracer concentration, here the dye gray scale. This area may be noncontiguous and the total A includes all "islands" in which the tracer concentration c is greater than or equal to C . Because $A(C, t)$ is a single-valued function, the inverse function $C(A, t)$ can also be defined. If the advection–diffusion equation

$$\frac{\partial c}{\partial t} + J[\psi, c] = \kappa \nabla^2 c + S \quad (1)$$

is integrated over $A(C, t)$ and the condition of incompressibility is used, the resulting constraint can be written, after some manipulation, as

$$\frac{\partial C(A, t)}{\partial t} = \frac{\partial}{\partial A} \left[\kappa L_e^2 \frac{\partial}{\partial A} C(A, t) \right]. \quad (2)$$

The source term S in (1) has been neglected as we consider tracer distributions only after injection has been terminated. The diffusion coefficient $\kappa_{\text{eff}} = \kappa L_e^2$ in (2) is the product of the molecular or subgrid-scale diffusivity κ and the square of the *effective length*, defined by

$$L_e^2 = \frac{\langle |\nabla c|^2 \rangle}{(\partial C / \partial A)^2}. \quad (3)$$

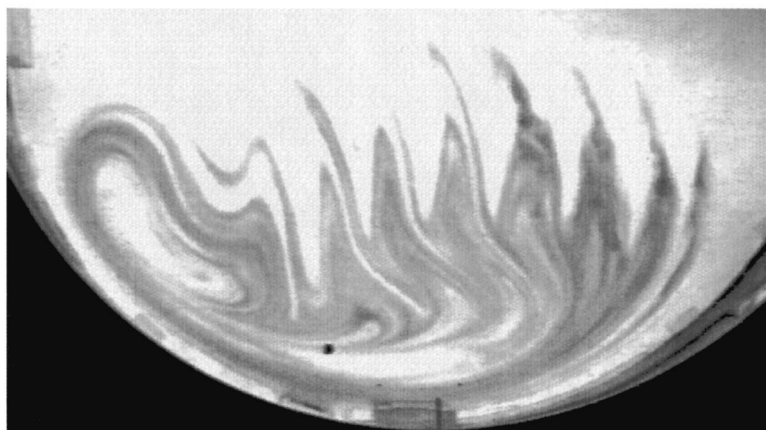
The operator $\langle (\cdot) \rangle$ denotes average over the area between adjacent tracer contours and is defined by

$$\langle (\cdot) \rangle = \frac{\oint (\cdot) \frac{dl}{|\nabla c|}}{\oint \frac{dl}{|\nabla c|}} \quad \text{or, equivalently} \quad (4a)$$

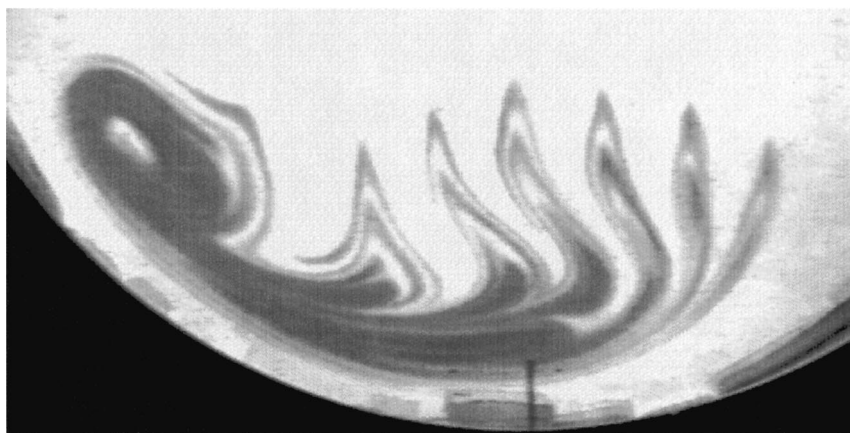
$$\langle (\cdot) \rangle = \frac{\partial}{\partial A} \iint (\cdot) dA. \quad (4b)$$

In essence, (1) has been reduced to a diffusion equation in A -space in which the effect of advection is contained in the diffusion coefficient κL_e^2 . The effective length L_e is a measure the convolution of the tracer contours, and will grow as the tracer is stirred. Here L_e is not the actual length L of the contour; however, it can be shown (Haynes and Shuckburgh 2000a) that $L_e > L$. When κ_{eff} is plotted as a function of A (or C), minima generally correspond to barriers to mixing whereas maxima correspond to regions of active transport and mixing. These relationships are most meaningful if κ_{eff} is independent of the initial tracer field, a situation that can often be realized by allowing the tracer to spread and mix to the point where it is uniformly distributed along, but not across, the time-average streamlines of the flow. Haynes and Shuckburgh (2000a,b) note that an adjustment period of about a month is required in simulations of the stratosphere. Generally speaking, the magnitude of κ_{eff} is interesting only in comparison between different experiments. Since κ is constant in our laboratory tank, further discussion is limited to comparisons of L_e distributions.

a.



b.



c.

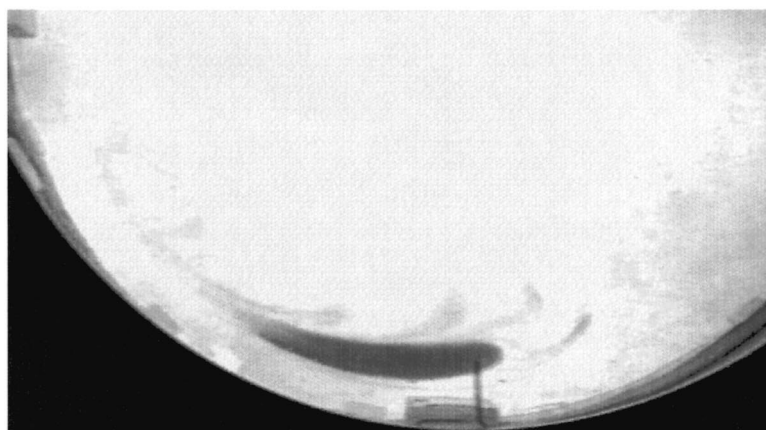


FIG. 10. Dye patterns found for the case $\delta = 1.25$ and $A_{osc} = 0.05$ with (a) injection in the western boundary current just to the west of the southern gyre; (b) injection just inside the edge of the southern gyre; (c) injection well inside the southern gyre. North is to the left.

Our use of effective diffusivity is a bit different from what has just been described. We wish to compare the magnitude of mixing in a bulk sense between time-dependent single- and double-recirculation gyres. The presence of hyperbolicity in the latter but not the former suggest that L_e should be noticeably higher on average in the latter. Calculations of L_e are made at times shorter⁶ than the adjustment period suggested above, and the results are therefore sensitive to how the dye is introduced. Comparisons between experiments were therefore made using identical injection times and rates, and by maintaining the injection point at a fixed location (or, in some cases, at what was judged to be fixed relative to the edge of the recirculation). The experimentally determined $L_e^2(C)$ is typically noisy compared to that obtained in numerical simulations (e.g., Nakamura 1996; Haynes and Shuckburgh (2000a,b) where the initial tracer distribution is smooth and where a longer adjustment period is allowed for. The noise level of our distributions is large enough to make identification of barriers difficult, but weak enough to render comparisons of different experiments meaningful.

b. Procedure

Effective diffusivity can be calculated from a snapshot of the tracer (dye) field and the calculation itself includes only integrals and derivatives with respect to the area A within contours if the definition (4b) is used. The function $A(C)$ is constructed by counting for each C the number of gray-scale pixel values greater than C and multiplying by the area-to-pixel ratio. In addition, a $|\nabla c|^2$ value is estimated for each pixel using a second-order centered difference approximation. These values are summed to form the area integral in the expression for $\langle |\nabla c|^2 \rangle = \partial/\partial A \iint |\nabla c|^2 dA$. No contouring of C , nor calculation of line integrals is required.

Dye is typically injected into the tank at a constant rate at a fixed location for 23 min. All L_e^2 calculations are from images taken after the dye pump is stopped. In all cases the adjustment time is longer than the typical winding time (2–4 min in the northern gyre and 10 min in the southern gyre) of particles within recirculations. Although some vertical mixing and diffusion of the dye occurs, the visual evidence is that the dye became vertically homogenized within a 5–10 cm-thick layer about the level of the needle during the injection and adjustment time.

⁶ Practical considerations place a limit on the adjustment time for the dye. As the dye spreads out, it tends to wander into reaches of the tank not easily covered by our imaging system. In order to measure $A(C)$, it is necessary to have an image in which all C contours are closed, which is ensured when the dye has not spread to the edge of the image.

c. Results

Chaotic advection sets in above the transition from the unsteady single-gyre to the unsteady twin-gyre. To quantify the preferential stirring claimed to be due to chaotic advection, it necessary to show first that this increase is not due to the geometric transition alone (without time dependence). We do so by calculating $L_e^2(C)$ for a range of steady cases with increasing δ . The single- and twin-gyre cases $\delta = 1.00$ and $\delta = 1.25$ have very similar, if noisy, $L_e^2(C)$ (Fig. 11a). The results are based on images taken 31 min after injection was halted. By contrast, the introduction of time dependence (with $A_{\text{osc}} = 0.05$) leads to significant differences (Fig. 11b). An order of magnitude increase in the mean and peak values of L_e^2 occurs in the twin gyre ($\delta = 1.25$) case.

It can also be shown that increasing inertia in the *unsteady* single gyre does not significantly increase the stirring. When the mean values of L_e^2 are calculated over a range of δ , and with $A_{\text{osc}} = 0.05$ in each case, the resulting values (Fig. 12) are remarkably similar for all single-gyre cases ($\delta < 1.10$). Frames (a) and (b) show results based on data measured 32 and 54 min after injection is begun (and 9 min and 21 min after injection is terminated). Open circles indicate an injection point just inside the western or eastern edge of the southern gyre, while asterisks indicate injection well into the interior of the southern gyre. The setting $\delta = 1.12$, which is considered borderline between the two geometries, has similar values to those with lower δ . A significant jump in mean L_e^2 generally occurs upon transition to the twin gyre geometry ($\delta = 1.25$), particularly for dye injected just inside the edge of the southern gyre (open circles). Increased sensitivity to the injection point is also apparent at $\delta = 1.25$, but all cases with injection near the gyre edge are substantially larger than those for lower δ .

6. Discussion

Chaotic advection is a possible mechanism for fluid exchange and mixing among a western boundary current and adjacent recirculation gyres. Geometries favorable for this process contain a distinguished hyperbolic trajectory or at least a region of strong and persistent stretching and contraction, such as the self-intersection of our figure-eight gyre. In the presence of time-dependence, trajectories brought into close contact with a DHT tend to become chaotic. Lagrangian chaos in such a setting is limited to regions occupied by the folded and tangled stable and unstable manifolds of the DHT. Associated transport processes can be quantified by identifying turnstile lobes whose boundaries are defined by sections of the intersecting manifolds. We have attempted to visualize some of these objects through careful injection of dye in a laboratory model. The spreading of dye in the twin-gyre geometry has been compared to a single-gyre case that has no region of strong hy-

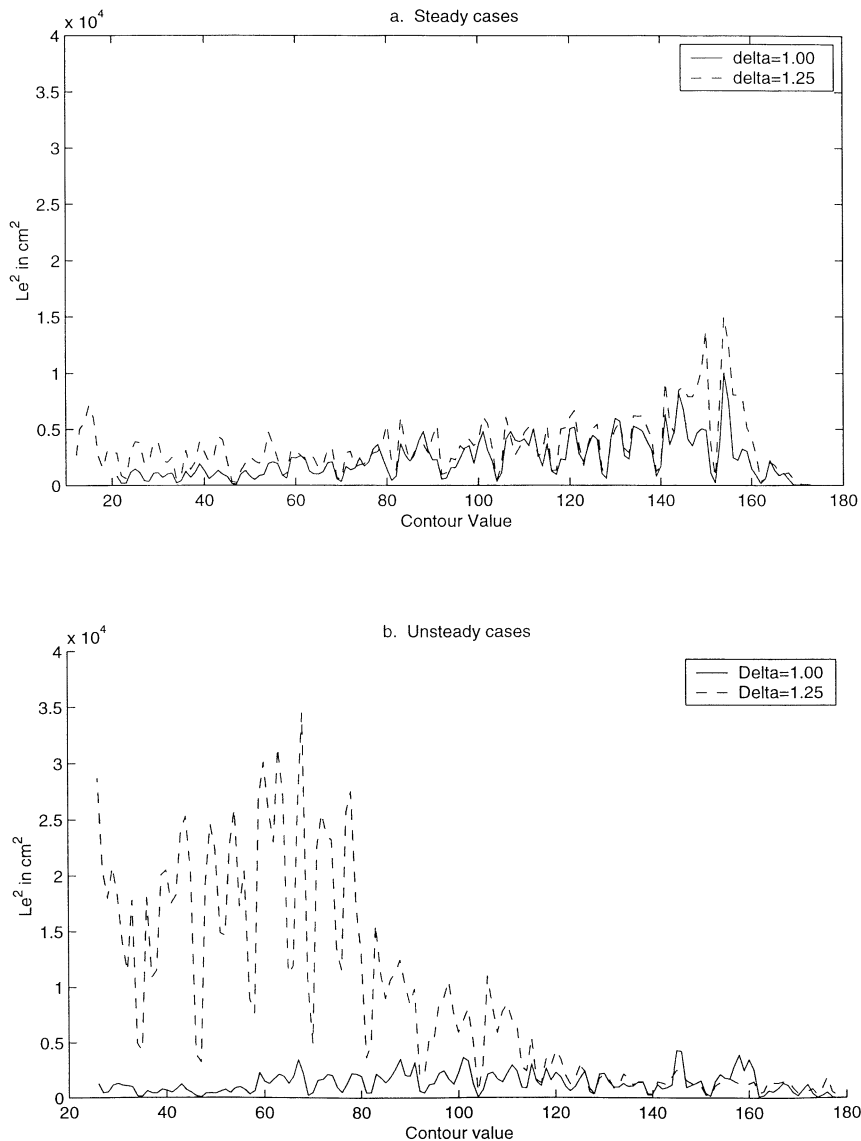


FIG. 11. (a) $L_e^2(C)$ for steady single ($\delta = 1.00$) and twin ($\delta = 1.25$) recirculation gyres. (b) $L_e^2(C)$ for the same cases but with unsteady forcing ($A_{osc} = 0.05$).

perbolicity and is therefore unfavorable for chaotic advection. Quantitative comparisons of mixing between the single- and twin-gyre cases have been made based on the effective diffusivity calculated from snapshots of the dye fields.

Both the visual and quantitative evidence suggests the presence of preferential exchange, stirring, and mixing in the twin-gyre case. The process by which western boundary layer fluid is advected into, and later expelled from, the northern member of the twin gyre is suggested by visualization of the unstable manifold (or something very close to it) of the northern gyre (Fig. 8). Also, by approximating a segment of the stable manifold using the principle of equal lobe areas, some of the lobes that deliver and export fluid to and from the northern gyre

can be visualized (Fig. 9) and the associated chaotic transport and flushing time estimated. The dye patterns also indicate barriers to transport in the middle of the gyres, as evidenced by the clear region in the northern gyre (Fig. 7c or 10a,b) and the trapped dye in the center of the southern gyre (Fig. 10c). Long-term snapshots of the dye (e.g., Fig. 10) suggest how tracers are transported into the interior basin circulation. Measurements of the effective length L_e (that appears in the definition of effective diffusivity $\kappa_{eff} = \kappa L_e^2$) confirm preferential stirring in the twin-gyre case as opposed to the single-gyre case. Unfortunately, the distributions of L_e^2 as a function of tracer concentration C are sufficiently noisy to preclude identification of barriers, as has been done in previous numerical studies.

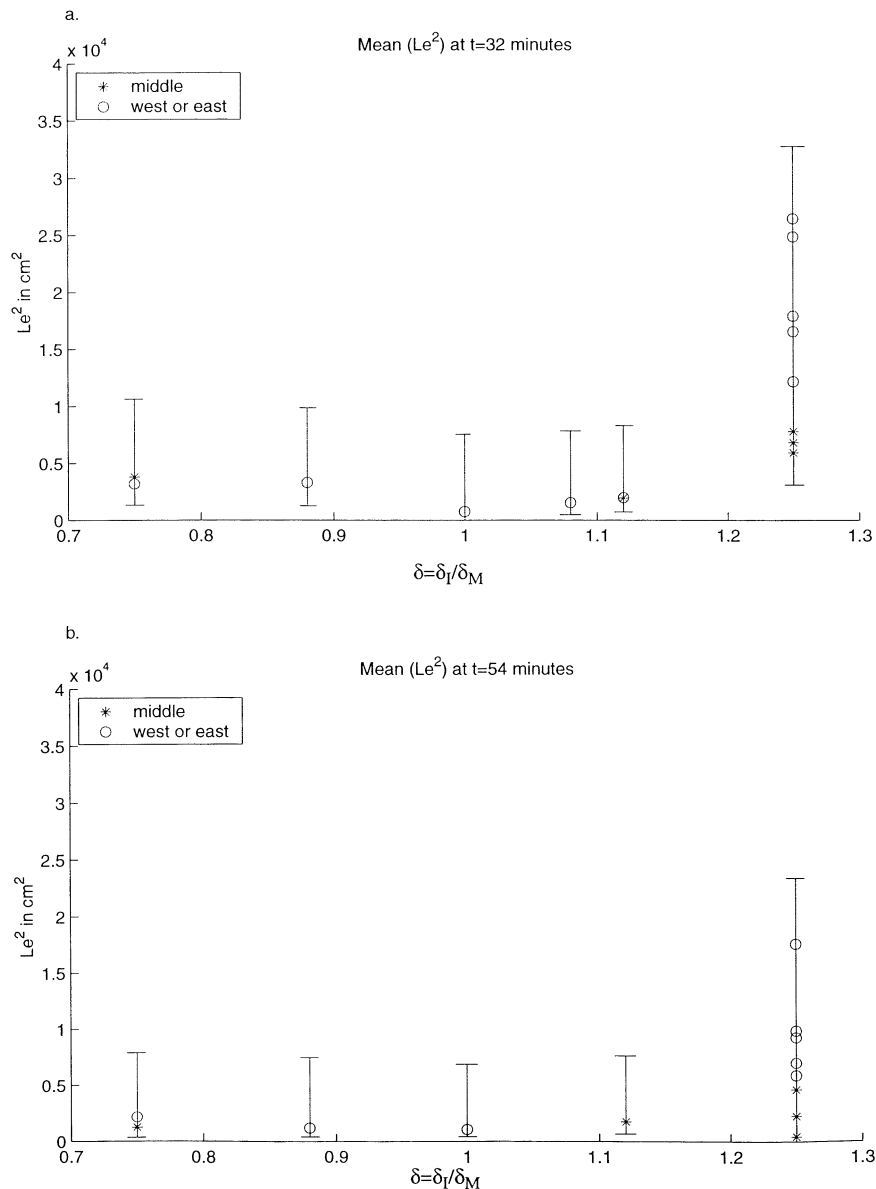


FIG. 12. Mean values of L_e^2 (cm^2) in unsteady cases presented as a function of $\delta = \delta_I / \delta_M$ and calculated at (a) $t = 32$ min and (b) 54 min. In all cases $A_{\text{osc}} = 0.05$. Open circles represent cases with dye injected into the western or eastern part of the southern recirculation and asterisks represent cases with dye injected into the very center of the southern recirculation. Bars represent qualitative estimates of uncertainty based on cases in which runs were repeated several times.

Examples of chaotic advection are often characterized by a separation between Lagrangian and Eulerian time-scales, with $T_L \ll T_E$. In fact, this scale separation is sometimes taken as one of the defining characteristics of chaotic advection (Shepherd et al. 2000). An interpretation of this requirement is that the local hyperbolicity underpinning Lagrangian chaos must persist over many “winding” times of the particle motion. A pair of closely spaced parcels will therefore travel through the flow field, occasionally wandering close enough to

a hyperbolic region that exponential separation occurs. This picture provides a connection with conventional chaotic behavior, a connection that would become more tenuous, and perhaps lost, if the hyperbolic regions were to rapidly disappear and reform. The requirement $T_L \ll T_E$ is therefore made under the expectation that the Lagrangian motion will live in a slowly varying Eulerian velocity field and that, in particular, the hyperbolic regions will be long lived. Shepherd et al. (2000) argue that the stratosphere (a region where chaotic advection

is thought to be relevant) is characterized by $T_L \ll T_E$, whereas the mesosphere (where chaotic advection is a poor model for stirring) is characterized by $T_L \cong T_E$.

It is also possible, however, for persistent hyperbolic structures to exist in flows where $T_L \cong T_E$. Examples can be arranged by tuning parameters in simple models (e.g. Bower 1991; Samelson 1992; Pratt et al. 1995). Though $T_L \cong T_E$ in our experiment, the flow is apparently characterized by persistent strong hyperbolicity in the twin-gyre configuration. Thus, many of the Lagrangian objects that typify chaotic advection (manifolds, lobes, barriers, etc.) can still be found.

Although visual evidence (e.g., Figs. 10a,b) suggests that exchange between the gyres and their surroundings occurs to the east of the gyres, such a judgment is entirely subjective. A boundary for the recirculation can be defined as the union of segments of the stable and unstable manifolds (Fig. 2c or 2d). The intersection point at which the segments are joined can be chosen in many ways and one's interpretation of where fluid enters and leaves the recirculation depends on this choice. For example, joining the stable and unstable manifolds at the intersection between lobes A' and B in Fig. 2c would formally lead to exchange across the western side of the gyre. In the laboratory gyre, the lobes at the western side are undoubtedly narrow and elongated, a feature associated with the relatively high fluid speeds in this region. The lobes here are defined primarily by the highly convoluted stable manifold, which is hidden in our images. On the eastern side of the gyre, where the stable manifold has relatively little curvature, the lobes are defined primarily by the highly convoluted and easily visualized unstable manifold. The resulting picture is one in which the lobes are more apparent at the eastern side of the gyre, giving the impression that exchange occurs there. A sound way of thinking about the exchange is that its location depends on how the boundary is defined but that its magnitude does not. Having said this, it is also apparent from the experiments that the zonal spreading of a tracer away from the western boundary is most rapid in the region to the east of the twin gyres.

The present work has suggested chaotic advection as a possible mechanism for transport and mixing within and between boundary currents and recirculations. However, the relevance of this mechanism in the ocean has not been established. In the search through spatial scales over which chaotic advection might be important, the focus should be on motions that are quasi-two-dimensional, either horizontally or along isopycnals. Given an isopycnal velocity field containing mesoscale features, say, it would probably not be hard to find coherent eddies or recirculations that might serve as the organizing structures for chaotic advection. Further, it should be possible to locate hyperbolic trajectories within such flow fields and to plot their stable and unstable manifolds, at least over finite spans in time. [Kuznetsov et al. (2000, submitted to *J. Phys. Oceanogr.*) have done

just this using a numerical model of the Gulf of Mexico circulation.] However, proof that chaotic advection is relevant requires more than just formal identification of these objects. The organizing structures and their hyperbolic trajectories must be persistent. Moreover, the manifolds must be distinct and remain smooth on the scale of the organizing structures, indicating that advection by these structures, and not by smaller eddies, is responsible for the stretching and folding of fluid elements and the generation of tracer fine structure. In contrast, the stretching and folding in a conventional 2D turbulent enstrophy or energy cascade is strongly influenced by a range of eddy scales. Dye injected at a fixed location evolves into a plume, rather than the smooth filaments seen in Figs. 8 and 9. Hyperbolic trajectories are intermittent and their stable and unstable manifolds are indistinct and limited in length. In summary, the main challenge in establishing chaotic advection as an oceanographically relevant process is not in identifying organizing structures, hyperbolic trajectories, and the like, but rather in eliminating turbulence as the mechanism controlling transport and stirring.

Shepherd et al. (2000) discuss ways in which atmospheric data has been used to distinguish between chaotic advection and conventional turbulence. Wavenumber spectra provide a major basis for comparison. Since small-scale eddies are relatively unimportant in chaotic advection, the corresponding kinetic energy or passive tracer spectra tend to decay more steeply than those for classical turbulence. In the oceanographic context, such a comparison would require wavenumber spectra of these quantities along isopycnal surfaces. Such products are virtually unknown at present. Stammer (1997) has calculated global wavenumber spectra of kinetic energy based on satellite altimeter measurements. Over the range of resolvable scales of a few thousand to about 50 km, only the band 50–200 km indicates a decay steep enough to be a candidate for chaotic advection. However these data are based on measurements of sea surface height and do not directly relate to quasi-2D motion along particular isopycnal surfaces. Also, scales below the deformation radius, one of the most likely ranges of relevance for chaotic advection, are not resolved.

More promising discriminants might follow from the analysis of float and drifter data. The stirring associated with chaotic advection is much less homogeneous than that produced by conventional turbulence and this should show up in the statistics of dispersion. In principle, a pair of closely spaced floats launched in the (nonchaotic) center of either of the twin gyres will separate from each other at a rate linear in time. A similar pair launched in the (chaotic) region of tangled manifolds should experience separation at a rate exponential in time. As shown by Shepherd et al. (2000) the presence of distinct behavior in different regions of the flow field causes PDFs of measures of relative dispersion to be highly skewed. In conventional turbulence, which lacks barriers and islands of nonchaotic motion, floats are free

to sample the entire flow field and the resulting PDFs are much less skewed. To our knowledge, this idea has not been exploited in the analysis of ocean float and drifter data.

Acknowledgments. Deese was supported during the course of this work by a National Defense Science and Engineering Fellowship from the U.S. Department of Defense. Pratt was supported by a grant from the Office of Naval Research (N00014-99-1-0258) and Helfrich by a grant from the National Science Foundation (OCE-9616949). The authors wish to thank R. Beardsley, C. Cenedese, C. Mauritzen, M. McCartney, Robert Pickart, A. Rogerson, J. Salzig, F. Straneo, J. Wells, and two anonymous reviewers for helpful suggestions and assistance that was given during the course of this work.

APPENDIX

Technical Information

a. Video and laser

The Pulnix video camera was attached to a frame rotating with the table so that images are stationary with respect to the tank. The neutrally buoyant particles were illuminated using a 6 W argon ion laser mounted away from the rotating table. The laser beam was transmitted through a fiber-optic cable and rotating coupling onto the table. A specialized lens brought the beam into a horizontal sheet of light, which was shone through the tank about 5 cm below the lid. To visualize dye, two 20 W fluorescent lightbulbs were positioned facing upward below the tank. Blackout cloths were suspended from the ceiling and pinned around the tank to cut down as much as possible on background light. Images were recorded on a VCR and digitized using Mutech Mv-1000 digital imaging software.

b. Neutrally buoyant particles

In order to match the density of the particles to the density of the liquid in the tank, we used Pliolite plastic particles ($\rho = 1.024 \text{ kg m}^{-3}$) and saltwater ($\rho \cong 1.022 \text{ kg m}^{-3}$) filtered at $50 \mu\text{m}$. These particles were hand ground with a mortar and pestle and then sorted into size classes using a series of sieves. Particles of diameter $d \geq 250 \mu\text{m}$ were chosen to make streak diagrams and particles of diameter $150 \mu\text{m} \leq d \leq 250 \mu\text{m}$ were chosen for PIV analysis.

c. Spinup

Twelve minutes of spinup time was allowed for all runs. This time was much longer than the viscous spinup time $E_k^{-1/2} f^{-1} \cong 60 \text{ s}$ and the $\cong 30 \text{ s}$ time required for the fastest Rossby wave to cross the tank. Unsteadiness in the flow was not visually observed after 7 or 8 min.

d. Dye injection

We used McCormick red food coloring $\rho = 1.02391 \text{ (kg m}^{-3}\text{)}$ diluted to match the $\rho \cong 1.022 \text{ (kg m}^{-3}\text{)}$ tank water at 20°C . This mixture sat in a reservoir (on the rotating table) and was pumped through tygon tubing and into the feed needle by a variable flow, peristaltic pump. This Variable Flow Mini Pump fed the dye flow through a section of 0.14-cm diameter tubing at a rotor rpm ~ 0.5 . This results in a calculated flow rate of approximately $6 \times 10^{-3} \text{ cm s}^{-1}$, which would result in a total input of 8 cm^3 over the course of each run. As Figs. 5, 8, and 9 show, dye leaves the needle and enters the fluid at nearly a right angle to the needle (approximately parallel to the western boundary current flow) implying minimal disturbance of the ambient velocity field by the dye stream.

e. PIV analysis and lobe dynamics

In principle, PIV velocities could be obtained over the entire tank at regular time slices. If the flow were exactly periodic in time, data acquired over one period would provide gridded velocities for all space and time, raising the possibility of performing a lobe analysis. Miller et al. (1977) carried out a similar analysis using nearly periodic data obtained from a numerical model of a meandering jet. The lack of exact time periodicity leads to small discontinuities at the end of each nominal time period. Willingness to live with the associated errors allows turnstile lobes to be tracked over several periods. The lobes tend to be stretched into fine filaments whose width rapidly decreases to below that afforded by the numerical resolution.

The observed lobes have dimensions of 1–2 cm (Fig. 9). The darkened lobe in frame *a* evolves over one forcing period (T_{osc}) into something close to the darkened lobe in frame *c*. After the next period, this lobe is then stretched at a rate that causes its width to decrease to a fraction of a centimeter over the next T_{osc} (Fig. 8). Lobes that are entering the northern gyre (e.g., Fig. 9a) presumably evolve from very thin lobes carried north by the western boundary layer. Some of this fluid may have been expelled from the southern gyre. It would be interesting to follow all of these lobes backward and forward in time to learn more about the origin and fate of fluid that is carried into and out of the northern gyre. Unfortunately, the camera resolution and PIV algorithm allows velocities to be measured with a spatial resolution of at best 1 cm, lower than required to resolve the highly filamented lobes.

REFERENCES

- Beardsley, R. C., 1969: A laboratory model of the wind-driven ocean circulation. *J. Fluid Mech.*, **38**, 255–271.
 Bower, A. S., 1991: A simple kinematic mechanism for mixing fluid parcels across a meandering jet. *J. Phys. Oceanogr.*, **21**, 173–180.

- , and H. D. Hunt, 2000a: Lagrangian observations of the Deep Western Boundary Current in the North Atlantic Ocean. Part I: Large-scale pathways and spreading rates. *J. Phys. Oceanogr.*, **30**, 764–783.
- , and —, 2000b: Lagrangian observations of the Deep Western Boundary Current in the North Atlantic Ocean. Part II: The Gulf Stream–Deep Western Boundary Current crossover. *J. Phys. Oceanogr.*, **30**, 784–804.
- Deese, H. E., 2001: Chaotic advection and mixing in a Western Boundary Current–recirculation system: Laboratory experiments. M.S. thesis, Woods Hole Oceanographic Institution–MIT Joint Program, 118 pp.
- Fine, R. A., 1995: Tracers, time scales and the thermohaline circulation: The lower limb in the North Atlantic Ocean. *Rev. Geophys.*, **33** (Suppl.), 1353–1365.
- Friedrichs, A. M., and M. M. Hall, 1993: Deep circulation in the tropical North Atlantic. *J. Mar. Res.*, **51**, 697–736.
- Griffiths, R. W., and A. E. Kiss, 1999: Flow regimes in a wide “sliced-cylinder” model of homogeneous beta-plane circulation. *J. Fluid Mech.*, **399**, 205–236.
- Haynes, P., 1999: Transport, stirring, and mixing in the atmosphere. *Chaos and Turbulence*, H. Chaté, E. Villermaux, and J.-M. Chomaz, Eds., Kluwer, 406 pp.
- , and E. Shuckburgh, 2000a: Effective diffusivity as a diagnostic of atmospheric transport. Part I: Stratosphere. *J. Geophys. Res.*, **105** (D18), 22 777–22 794.
- , and —, 2000b: Effective diffusivity as a diagnostic of atmospheric transport. Part II: Troposphere and lower stratosphere. *J. Geophys. Res.*, **105** (D18), 22 795–22 810.
- Hogg, N. G., 1992: On the transport of the Gulf Stream between Cape Hatteras and the Grand Banks. *Deep-Sea Res.*, **39**, 1231–1246.
- Ide, K., F. Lekien, and S. Wiggins, 2001: Distinguished hyperbolic trajectories in time dependent fluid flows: Analytical and computational approach for velocity fields defined as data sets. *Nonlinear Proc. Geophys.*, in press.
- Johns, E., R. A. Fine, and R. L. Molinari, 1997: Deep flow along the Western Boundary south of the Blake Bahama Outer Ridge. *J. Phys. Oceanogr.*, **27**, 2187–2208.
- Kuznetsov, L., M. Toner, A. D. Kirwan, C. K. R. T. Jones, L. Kantha, and J. Choi, 2001: The Loop Current and adjacent rings delineated by Lagrangian analysis. *J. Phys. Oceanogr.*, submitted.
- Lavender, K. L., R. E. Davis, and W. B. Owens, 2000: Mid-depth recirculation observed in the interior Labrador and Irminger Seas by direct velocity measurements. *Nature*, **407**, 66–69.
- Leaman, K. D., and P. S. Vertes, 1996: Topographic influences on recirculation in the Deep Western Boundary Current: Results from RAFOS float trajectories between the Blake–Bahama Outer Ridge and the San Salvador “gate.” *J. Phys. Oceanogr.*, **26**, 941–960.
- Lee, T. N., W. E. Johns, R. J. Zantopp, and E. R. Fillenbaum, 1996: Moored observations of Western Boundary Current variability and thermohaline circulation at 26.5°N in the subtropical North Atlantic. *J. Phys. Oceanogr.*, **26**, 962–982.
- Malhotra, N., and S. Wiggins, 1998: Geometric structures, lobe dynamics, and Lagrangian transport in flows with aperiodic time-dependence, with applications to Rossby wave flow. *J. Nonlinear Sci.*, **8**, 401–456.
- McCartney, M. S., 1992: Recirculating components to the deep boundary current of the northern North Atlantic. *Progress in Oceanography*, Vol. 29, Pergamon Press, 283–383.
- Meacham, S. P., and P. S. Berloff, 1997: Instabilities of a steady, barotropic, wind-driven circulation. *J. Mar. Res.*, **55**, 885–913.
- Miller, P. D., C. K. R. T. Jones, A. M. Rogerson, and L. J. Pratt, 1997: Quantifying transport in numerically-generated velocity fields. *Physica D*, **110**, 105–122.
- , L. J. Pratt, K. R. Helfrich, and C. K. R. T. Jones, 2002: Chaotic transport of mass and potential vorticity for an island recirculation. *J. Phys. Oceanogr.*, **32**, 80–102.
- Molinari, R. L., R. A. Fine, W. D. Wilson, R. G. Curry, J. Abell, and M. S. McCartney, 1998: The arrival of recently formed Labrador Sea Water in the Deep Western Boundary Current at 26.5°N. *Geophys. Res. Lett.*, **25**, 2249–2252.
- Nakamura, N., 1996: Two-dimensional mixing, edge formation, and permeability diagnosed in an area coordinate. *J. Atmos. Sci.*, **53**, 1524–1537.
- , and J. Ma, 1997: Modified Lagrangian-mean diagnostics of the stratospheric polar vortices. Part 2: Nitrous oxide and seasonal barrier migration in the cryogenic limb array etalon spectrometer and SKYHI general circulation model. *J. Geophys. Res.*, **102** (D22), 25 721–25 735.
- Pedlosky, J., and H. P. Greenspan, 1967: A simple laboratory model for the oceanic circulation. *J. Fluid Mech.*, **27**, 291–304.
- Pickart, R. S., and N. G. Hogg, 1989: A tracer study of the deep Gulf Stream cyclonic recirculation. *Deep-Sea Res.*, **36**, 935–956.
- , —, and W. M. Smethie Jr., 1989: Determining the strength of the Deep Western Boundary Current using the Chlorofluoromethane ratio. *J. Phys. Oceanogr.*, **19**, 940–951.
- Pratt, L. J., M. S. Lozier, and N. Beliakova, 1995: Parcel trajectories in quasigeostrophic jets: Neutral modes. *J. Phys. Oceanogr.*, **25**, 1451–1466.
- Raffel, M., C. Willert, and J. Kompenhans, 1998: *Particle Image Velocimetry: A Practical Guide*. Springer-Verlag, 253 pp.
- Rhein, M., 1994: The Deep Western Boundary Current: Tracers and velocities. *Deep-Sea Res.*, **41**, 263–282.
- Rogerson, A. M., P. D. Miller, L. J. Pratt, and C. K. R. T. Jones, 1999: Lagrangian motion and fluid exchange in a barotropic meandering jet. *J. Phys. Oceanogr.*, **29**, 2635–2655.
- Rom-Kedar, V., and S. Wiggins, 1990: Transport in two-dimensional maps. *J. Arch. Ration. Mech. Anal.*, **109**, 239–298.
- Samelson, R. M., 1992: Fluid exchange across a meandering jet. *J. Phys. Oceanogr.*, **22**, 431–440.
- Schmitz, W. J., and M. S. McCartney, 1993: On the North Atlantic Circulation. *Rev. Geophys.*, **31**, 29–49.
- Shepherd, T. G., J. N. Koshyk, and K. Ngan, 2000: On the nature of large-scale mixing in the stratosphere and mesosphere. *J. Geophys. Res.*, **105**, 12 433–12 446.
- Stammer, D., 1997: Global characteristics of ocean variability estimated from regional TOPEX/Poseidon altimeter measurements. *J. Phys. Oceanogr.*, **27**, 1743–1769.
- Thompson, L., 1995: The effect of continental rises on the wind-driven ocean circulation. *J. Phys. Oceanogr.*, **25**, 1296–1316.
- Watts, D. R., 1991: Equatorward currents in the temperature range 1.8°–6°C on the continental slope in the mid-Atlantic Bight. *Proc. Deep Convection and Deep Water Formation Workshop*, Vol. 51, Monterey, CA, Naval Postgraduate School, 183–196.
- Wiggins, S., 1992: *Chaotic Transport in Dynamical Systems*. Vol. 2, *Interdisciplinary Applied Mathematics*, Springer-Verlag, 301 pp.
- Winters, K., and E. D’Asaro, 1996: Diascalar flux and the rate of fluid mixing. *J. Fluid Mech.*, **317**, 179–193.